catalysts

MDPI

*Article*

# Dimethyl Ether Oxidation over Copper Ferrite Catalysts

**Maria Smyrnioti [1,2] and Theophilos Ioannides [1,*]**

[1] Foundation for Research & Technology-Hellas, Institute of Chemical Engineering Sciences (FORTH/ICE-HT), GR-26504 Patras, Greece; msmyrnioti@iceht.forth.gr
[2] Department of Chemistry, University of Patras, GR-26504 Patras, Greece
* Correspondence: theo@iceht.forth.gr

**Abstract:** The depletion of fossil energy sources and the legislation regarding emission control demand the use of alternative fuels and rapid progression of aftertreatment technologies. The study of dimethyl ether (DME) catalytic oxidation is important in this respect, as DME is a promising clean fuel and at the same time a VOC pollutant present in the tail gases of industrial processes. In the present work, copper ferrite catalysts synthesized via the citrate complexation method have been evaluated in DME oxidation. $N_2$-physisorption, XRD, $H_2$-TPR, and XPS were employed for the characterization of the mixed oxide catalysts. The copper ferrite spinel phase was detected in all samples accompanied by a gradual decrease in the bulk CuO phase upon increase in iron content, with the latter never vanishing completely. The $Fe_{0.67}Cu_{0.33}$ catalyst exhibited the highest catalytic activity in DME oxidation, attaining approximately a 4-fold higher oxidation rate compared to the respective pure copper and iron oxides. The enhanced catalytic performance was attributed to the higher specific surface area of the catalyst and its enhanced redox properties. Highly dispersed copper species were developed owing to the formation of the spinel phase. DME-TPD/TPSR experiments showed that the surface lattice oxygen of the $Fe_{0.67}Cu_{0.33}$ catalyst can oxidize preadsorbed DME at a lower temperature than all other catalysts which is in agreement with the $H_2$-TPR findings.

**Keywords:** dimethyl ether; oxidation; VOC; iron oxide; copper oxide; copper ferrite



**Citation:** Smyrnioti, M.; Ioannides, T. Dimethyl Ether Oxidation over Copper Ferrite Catalysts. *Catalysts* **2022**, *12*, 604. https://doi.org/10.3390/catal12060604

Academic Editors: Yanliu Dang, Zhu Luo, Shaopeng Rong, Jianhang Shi, Jinlong Wang, Tongzhou Xu and Xuehua Zou

Received: 29 April 2022
Accepted: 31 May 2022
Published: 2 June 2022



## 1. Introduction

Currently, the consumption of fossil energy sources in conjunction with the strict regulations concerning stationary and automotive emissions impose actions in two directions: utilizing green alternative fuels and improving aftertreatment technologies. Dimethyl ether (DME) can be produced from biomass or conventional feedstocks and has been proposed as a sustainable candidate to replace diesel fuel, while it also has similar physical properties to liquified petroleum gas (LPG) [1–3]. High energy density, high hydrogen to carbon ratio, high cetane number (>55), great compression ignition properties, ease in transportation/handling, and adaptability in the existing infrastructure are the main advantageous characteristics of DME [2]. DME-fueled engines result in lower CO, hydrocarbons, $NO_X$, and soot emissions compared to diesel ones [4]. Additionally, DME is converted into liquid at a pressure of 5 bar and it can easily be supplied to fuel processors [5,6]. Nonetheless, DME is also encountered in small amounts in flue gases of industrial processes, e.g., formaldehyde plants [7].

Catalytic oxidation (incineration) is an important process for emission control. Typically, noble metal-based catalysts are employed in CO and VOC abatement [8–12]. DME oxidation over $Pt/Al_2O_3$ has been reported by Ishikawa et al. [13]. Solymosi et al. investigated DME oxidation over Pt, Ru, Ir, Rh, and Pd supported on $Al_2O_3$ and found that the best-performing catalysts were $Ru/Al_2O_3$ and $Pt/Al_2O_3$ achieving complete DME oxidation at 400 °C [14]. $Au/ZrO_2$ and $Au/TiO_2$ modified with $CeO_2$ were investigated in DME oxidation by Idakiev et al. and the employed catalysts did not achieve complete DME conversion at temperatures up to 380 °C [15]. The main drawbacks of noble metal catalysts

are their scarcity and the fluctuations of their price, making them an expensive investment for industry; hence, effort has been made towards the development of cost-effective and active non-noble metal-containing catalysts. Transition metal oxides have been extensively investigated as potential catalysts for CO and VOC oxidation [5,16–20]. It has been reported that the combination of at least two metal oxides results in enhanced catalytic performance originating from synergistic effects and modified physicochemical properties, namely improved reducibility, higher concentration of lattice defects and oxygen vacancies, and enhanced stability provoked by the different ionic radii of the metal cations and the metal–metal or metal–oxygen–metal interactions [21–24].

Spinels with a general $AB_2O_4$ formula (where A and B are metal cations occupying tetrahedral and octahedral interstitial sites, respectively) are an important category of mixed transition metal oxides finding various applications in heterogeneous catalysis, electrocatalysis, gas sensing, energy storage, environmental remediation, and electronic and magnetic devices [25–30]. Spinel ferrites, in particular, have been extensively investigated in oxidation reactions both in the gas and liquid phases including peroxymonosulfate, benzyl alcohol, formaldehyde, DME, toluene, isopropyl alcohol, CO oxidation, and others [31–37]. Spinel ferrites can crystallize in the normal spinel structure where all divalent cations occupy the tetrahedral sites ($A^{II}$) while the trivalent cations occupy the octahedral ones ($B^{III}$); otherwise, the inverse spinel structure is formed, where the divalent cations occupy half of the octahedral sites and the trivalent ones are equally distributed between the tetrahedral and octahedral sites ($A^{III}$, $B^{II,III}$) [38]. The transition between normal and inverse spinel formation is directly related to the crystal field stabilization energy of ions in tetrahedral and octahedral sites.

Among possible ferrites, copper ferrite ($CuFe_2O_4$) with an inverse spinel structure demonstrates promising results towards CO and VOC catalytic oxidation. Amini et al. reported on the catalytic performance of mesoporous copper ferrite and concluded that copper and iron acted synergistically leading to enhanced catalytic activity in low-temperature CO oxidation [37]. Liu et al. synthesized 3D-ordered macroporous ferrites as catalysts for CO and simultaneous CO–NO oxidation. $CuFe_2O_4$ exhibited the highest catalytic activity which was attributed to improved redox properties and increased surface oxygen concentration [39]. Copper ferrite catalysts prepared by a combustion method were evaluated in methanol, ethanol, and acetone oxidation [40]. The authors proposed the formation of oxygen vacancies as a possible cause for the superior catalytic performance of the $CuFe_2O_4$ catalyst. The catalytic oxidation of alcohols, namely methanol and isopropyl alcohol, over copper ferrite samples has also been reported by Tsoncheva et al. and Tu et al. [36,41].

Taking into consideration the existing information regarding the potential use of copper ferrite catalysts in various oxidation reactions including VOC, their application in DME oxidation would be of interest. To the best of our knowledge, there are no reports on DME oxidation over copper ferrite catalysts.

In the present work, $Fe_xCu_{1-x}$ catalysts have been synthesized via the citrate complexation method and have been evaluated in the gas-phase oxidation of dimethyl ether (DME). The effect of the presence of water vapor in the reactant feed has also been investigated. The best performing catalyst has been identified, while the prepared samples have been characterized by various techniques, including $N_2$ physisorption, powder-XRD, $H_2$-TPR, and XPS with the aim to establish a correlation between the catalytic activity and the physicochemical characteristics of the catalysts. In addition, DME-TPD and TPSR experiments have been employed to provide information regarding the interaction of DME with the surface of the catalyst.

## 2. Results

### *2.1. Textural and Structural Properties of $Fe_xCu_{1-x}$ Oxide Catalysts*

The $N_2$ adsorption–desorption hysteresis curves and the pore size distribution (PSD) of the $Fe_xCu_{1-x}$ samples and CuO and $Fe_2O_3$ single oxides are shown in Figure 1. According to the IUPAC classification, all isotherms can be classified as type II with H1 hysteresis

loops closing at $P/P_0 = 0.8$ while the samples contain both meso- and macropores based on the pore size distribution (Figure 1b). The specific surface area of the samples increases upon iron addition, reaching a maximum value of 33 $m^2\ g^{-1}$ for $Fe_{0.67}Cu_{0.33}$. The specific surface areas of the single oxides are lower than the mixed oxides, i.e., 17 $m^2\ g^{-1}$ for $Fe_2O_3$ and only 1.5 $m^2\ g^{-1}$ for CuO. Following the same trend, the total pore volume of the mixed oxides increases with increase in iron content, while the pure oxides exhibit lower total pore volume. The textural characteristics of the catalysts are summarized in Table 1.

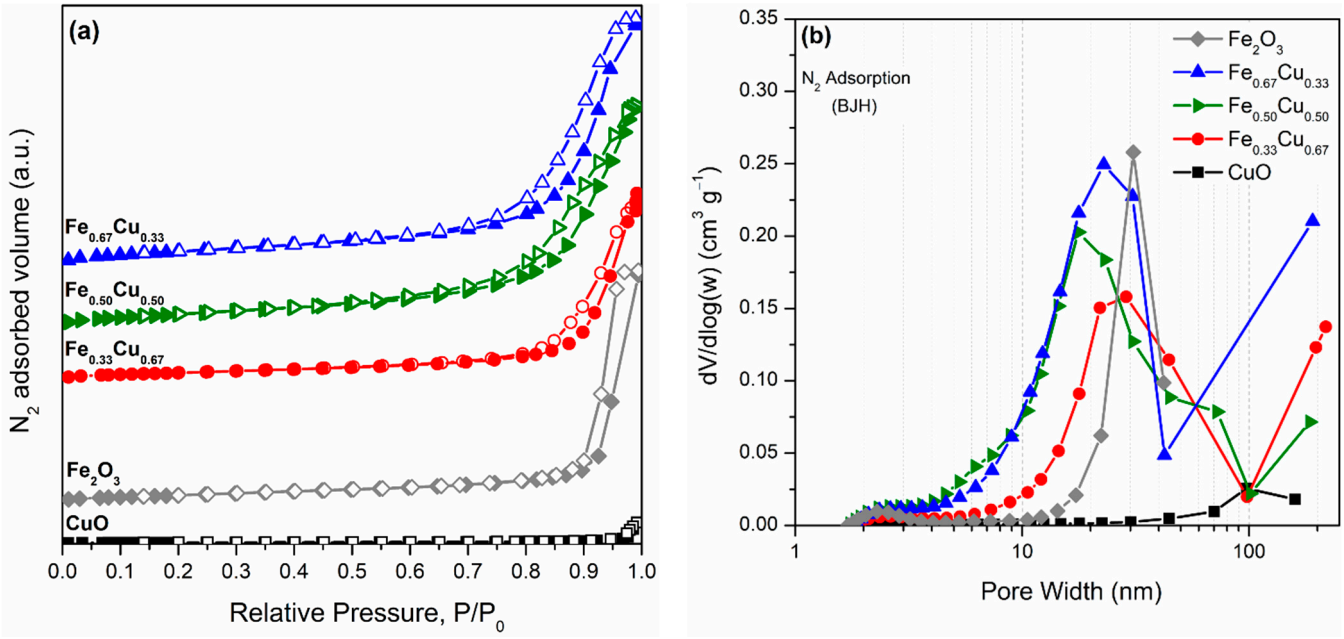


**Figure 1.** $N_2$ adsorption–desorption isotherms (**a**) and pore size distribution (**b**) of $Fe_xCu_{1-x}$ catalysts. The isotherms have been shifted vertically for clarity.

**Table 1.** Textural, structural, and redox characteristics of $Fe_xCu_{1-x}$ catalysts.

| Catalyst | $S_{BET}$ ($m^2\ g^{-1}$) | Pore Volume ($cm^3\ g^{-1}$) | Pore Diameter (nm) | Phase Composition | $d_{cryst}$ (nm) | $H_2$ Consumption (mmol $g_{cat}^{-1}$) |
|---|---|---|---|---|---|---|
| CuO | 1.5 | 0.013 | 9 | 100% (CuO) | 27.3 | 12.3 (12.6) * |
| $Fe_{0.33}Cu_{0.67}$ | 17 | 0.121 | 24 | 49.9% ($CuFe_2O_4$), 50.1% (CuO) | 14 ($CuFe_2O_4$), 17.7 (CuO) | 14.9 |
| $Fe_{0.50}Cu_{0.50}$ | 31 | 0.147 | 17 | 77.3% ($CuFe_2O_4$), 22.7% (CuO) | 10.4 ($CuFe_2O_4$), 16.6 (CuO) | 12.4 |
| $Fe_{0.67}Cu_{0.33}$ | 33 | 0.163 | 19 | 90.4% ($CuFe_2O_4$), 4.3% (CuO), 5.3% ($Fe_2O_3$) | 12.4 ($CuFe_2O_4$), 20.9 (CuO), 62.4 ($Fe_2O_3$) | 11.3 |
| $Fe_2O_3$ | 17 | 0.147 | 34 | 100% ($\alpha$-$Fe_2O_3$) | 39.8 | 13.3 (18.8) ** |

* Theoretical $H_2$ consumption (μmol $g_{cat}^{-1}$) $CuO \rightarrow Cu^0$. ** Theoretical $H_2$ consumption (μmol $g_{cat}^{-1}$) $Fe_2O_3 \rightarrow Fe^0$.

The crystal structure and phase composition of the $Fe_xCu_{1-x}$ samples were investigated by powder-XRD and the corresponding diffractograms are presented in Figure 2. CuO and $\alpha$-$Fe_2O_3$ diffractograms are also included for comparison. For all Fe-Cu mixed oxide samples, the reflections observed at $2\theta = 30.1$, 35.4, 37.1, 43.7, 53.5, 57, and 62.6° can be ascribed to the $CuFe_2O_4$ spinel phase displaying a cubic structure (PDF: 04-007-5166, space group: Fd-3m). Moreover, CuO was detected as a separate phase in all the examined samples. The sharp reflections at $2\theta = 35.5$, 38.7 and 48.7° are characteristic of the monoclinic CuO phase (PDF: 04-006-4186, space group: C2/c). Focusing on the characteristic reflection of CuO at $2\theta = 38.7°$, it is apparent that the increase in iron content of the mixed oxide catalysts results in a gradual decrease in the intensity of the CuO reflection apparently because more and more copper is involved in the formation of the cuprospinel

phase. Similar observations have been reported by Yeste et al. investigating copper–iron mixed oxide catalysts for CO-PROX reaction [42]. Nevertheless, the CuO reflection does not completely vanish even in the case of $Fe_{0.67}Cu_{0.33}$, thus copper cannot be fully incorporated into the $CuFe_2O_4$ structure with the residual copper forming a CuO separate phase. The additional phase of $\alpha$-$Fe_2O_3$, hematite (PDF: 04-003-1445, rhombic, space group: R-3c), was detected only in the case of $Fe_{0.67}Cu_{0.33}$ sample exhibiting a characteristic reflection at $2\theta = 33.1°$. The crystallite size of CuO, $CuFe_2O_4$, and $Fe_2O_3$ phases was calculated from the X-ray line broadening of the respective peaks at $2\theta = 38.7$, 30.1, and 33.1° and the results are summarized in Table 1. The crystallites size of the phases detected over the mixed Fe–Cu catalysts were in the range of 10–14 nm for $CoFe_2O_4$ and 16.5–21 nm for CuO whereas the crystallite size of the additional a-$Fe_2O_3$ phase in $Fe_{0.67}Cu_{0.33}$ was 62.4 nm. The minimum crystallite size overall was observed over the $Fe_{0.50}Cu_{0.50}$ sample. The calculated crystallite size of the single oxides was 27.3 nm for CuO and 39.8 nm for $Fe_2O_3$. Furthermore, the XRD diffractograms were Rietveld refined and the corresponding patterns are depicted in Figure S1. The percentage of each phase in $Fe_xCu_{1-x}$ samples was determined and the results are listed in Table 1. As expected, the addition of iron led to a gradual increase in the percentage of the spinel phase accompanied by the decrease of the bulk CuO phase, whereas the formation of $\alpha$-$Fe_2O_3$ was evident only in the $Fe_{0.67}Cu_{0.33}$ catalyst.

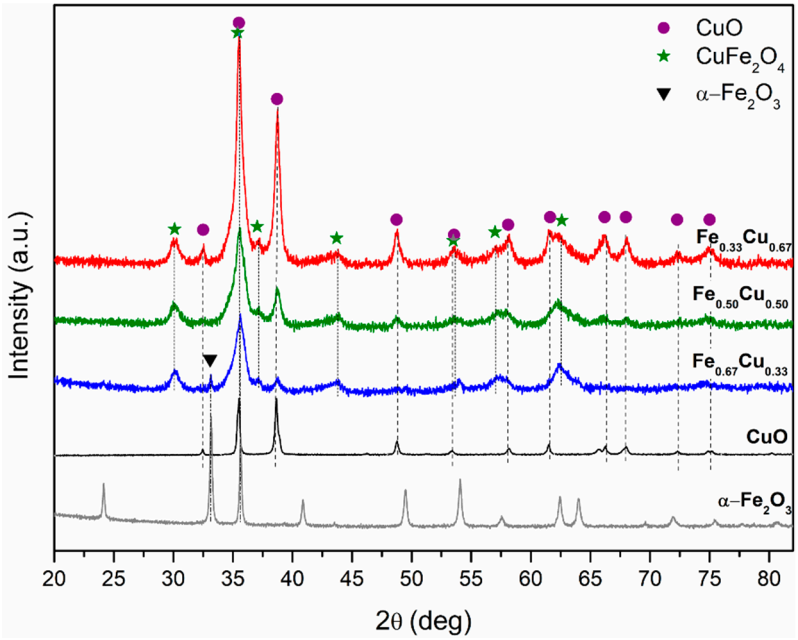


**Figure 2.** X-ray diffractograms of $Fe_xCu_{1-x}$ catalysts. CuO and $\alpha$-$Fe_2O_3$ are also included for comparison.

### *2.2. Reducibility of $Fe_xCu_{1-x}$ Oxide Catalysts*

The redox properties of $Fe_xCu_{1-x}$ samples were investigated employing $H_2$-TPR and the corresponding profiles are compiled in Figure 3. The pure CuO reduction profile exhibited a single peak centered at 325 °C, which is attributed to the overall reduction of CuO ($Cu^{2+}$) to metallic $Cu^0$ [43]. As the peak was not symmetrical, one can deduce that the reduction of CuO ($Cu^{2+}$) to $Cu_2O$ ($Cu^{1+}$) is also included in the lower temperature region. The $H_2$-TPR profile of pure $Fe_2O_3$ comprised a main peak centered at 395 °C assigned to the reduction of $Fe_2O_3$ to $Fe_3O_4$ while a subsequent broad peak initiating from 440 °C and not being completed up to 700 °C is attributed to the reduction of $Fe_3O_4$ to metallic Fe. Hematite ($\alpha$-$Fe_2O_3$) is reduced to metallic $Fe^0$ via the $Fe_3O_4 \rightarrow FeO \rightarrow Fe^0$ route, but the metastable FeO is not easily observed as it decomposes to $Fe_3O_4$ and metallic $Fe^0$ at temperatures lower than 620 °C [44,45]. $H_2$-TPR profiles of $Fe_{0.33}Cu_{0.67}$ and $Fe_{0.50}Cu_{0.50}$ are characterized by a main peak commencing above 100 °C followed by a broad shoulder

extending up to 600 °C or higher. It should be pointed out that it is not possible to delimit with certainty the reduction of each component due to the extensive overlap of the reduction peaks. Nonetheless, the main peak can be attributed to the reduction of CuO to $Cu^0$ as well as to the partial reduction of the cuprospinel phase ($CuFe_2O_4$). A small shoulder at 160–170 °C could be associated with the reduction of highly dispersed $Cu^{2+}$ species. The broad shoulder above 300 °C is ascribed to the subsequent bulk reduction of iron oxide species to metallic $Fe^0$. Regarding the $H_2$ consumption profile of $Fe_{0.67}Cu_{0.33}$, it is easy to distinguish at least three peaks in the low-temperature range (100–280 °C) ascribed to highly dispersed $Cu^{2+}$ species, bulk CuO reduction, and partial reduction of $CuFe_2O_4$ as well as reduction of $Fe_2O_3$ to $Fe_3O_4$, respectively, since, according to the XRD findings, $Fe_2O_3$ also exists as a separate phase in the $Fe_{0.67}Cu_{0.33}$ sample. As a general trend, the addition of iron leads to a systematic shift of the maxima of low-temperature peaks to lower temperatures. At the same time, the higher iron loading shifts the maxima of high-temperature shoulders to higher temperatures retarding the completion of the bulk reduction of iron species. Since the redox properties at the low-temperature region are linked to the catalytic activity in oxidation reactions, a close investigation of the reduction profiles in the temperature range of 30–200 °C will be useful. Figure 3b provides a magnification of the reduction profiles of the examined mixed oxide catalysts in the low-temperature range ($30 \leq T \leq 200$ °C). The rate of hydrogen consumption followed the order: $Fe_{0.67}Cu_{0.33}$ > $Fe_{0.50}Cu0_{0.50}$ > $Fe_{0.33}Cu_{0.67}$ >> CuO leading to the conclusion that the amount of highly dispersed $Cu^{2+}$ species arising from the development of spinel phase to a greater extent was higher over the $Fe_{0.67}Cu_{0.33}$ catalyst. These findings are supported by the phase composition percentages, taking into account the Rietveld refined XRD calculations. The experimental $H_2$ consumption is listed in Table 1. The theoretical $H_2$ consumption of CuO and $Fe_2O_3$ is also included in order to confirm the validity of the measurements. For CuO, the theoretical and experimental $H_2$ amounts are in total agreement whereas for $Fe_2O_3$, the experimental quantities are lower than the theoretical ones due to the incomplete reduction up to 700 °C, which was the upper temperature limit of the TPR runs.

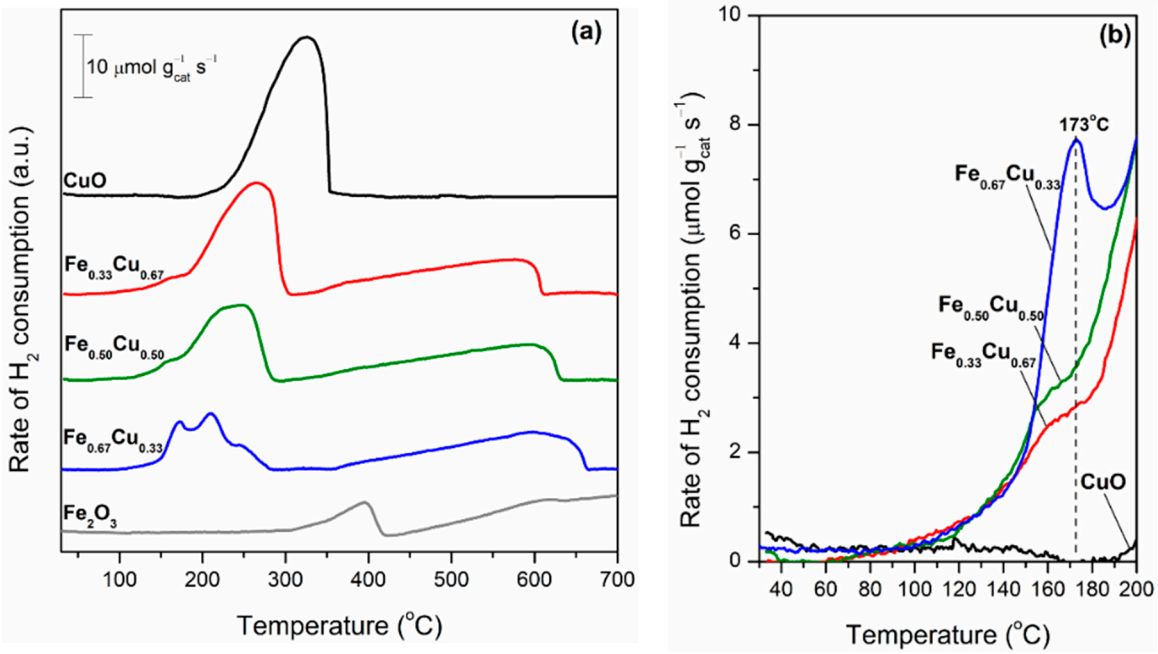


**Figure 3.** (**a**) $H_2$-TPR of $Fe_xCu_{1-x}$ catalysts and (**b**) magnification of $H_2$-TPR profiles in the temperature range $30 \leq T \leq 200$ °C.

### *2.3. XPS Measurements*

X-ray photoelectron spectroscopy was employed for the investigation of the surface oxidation state of $Fe_xCu_{1-x}$ catalysts. Cu 2p, Fe 2p, and O 1s core level spectra are depicted

in Figure 4. The Cu 2p XP spectra (Figure 4a) consist of two main peaks centered at 933.8 eV and 953.7 eV with a spin-orbit separation of 19.9 eV assigned to Cu $2p_{3/2}$ and Cu $2p_{1/2}$, respectively. The strong satellite peaks at ca. 942 eV and 962.2 eV are characteristic of the presence of $Cu^{2+}$ [46–48]. The only oxidation state of copper encountered was the +2 as manifested by the constant intensity ratios of the satellite feature with respect to the main photoelectron peak. The presence of $Cu^{+}$ would be accompanied by a decrease of the aforementioned ratio as weak satellite peaks are characteristic of monovalent copper, which is not the case in the present results. Additionally, the X-ray induced Auger electron spectra of the CuLVV region, centered at 917.8 eV, further confirm the $Cu^{2+}$ presence (Figure 4b).

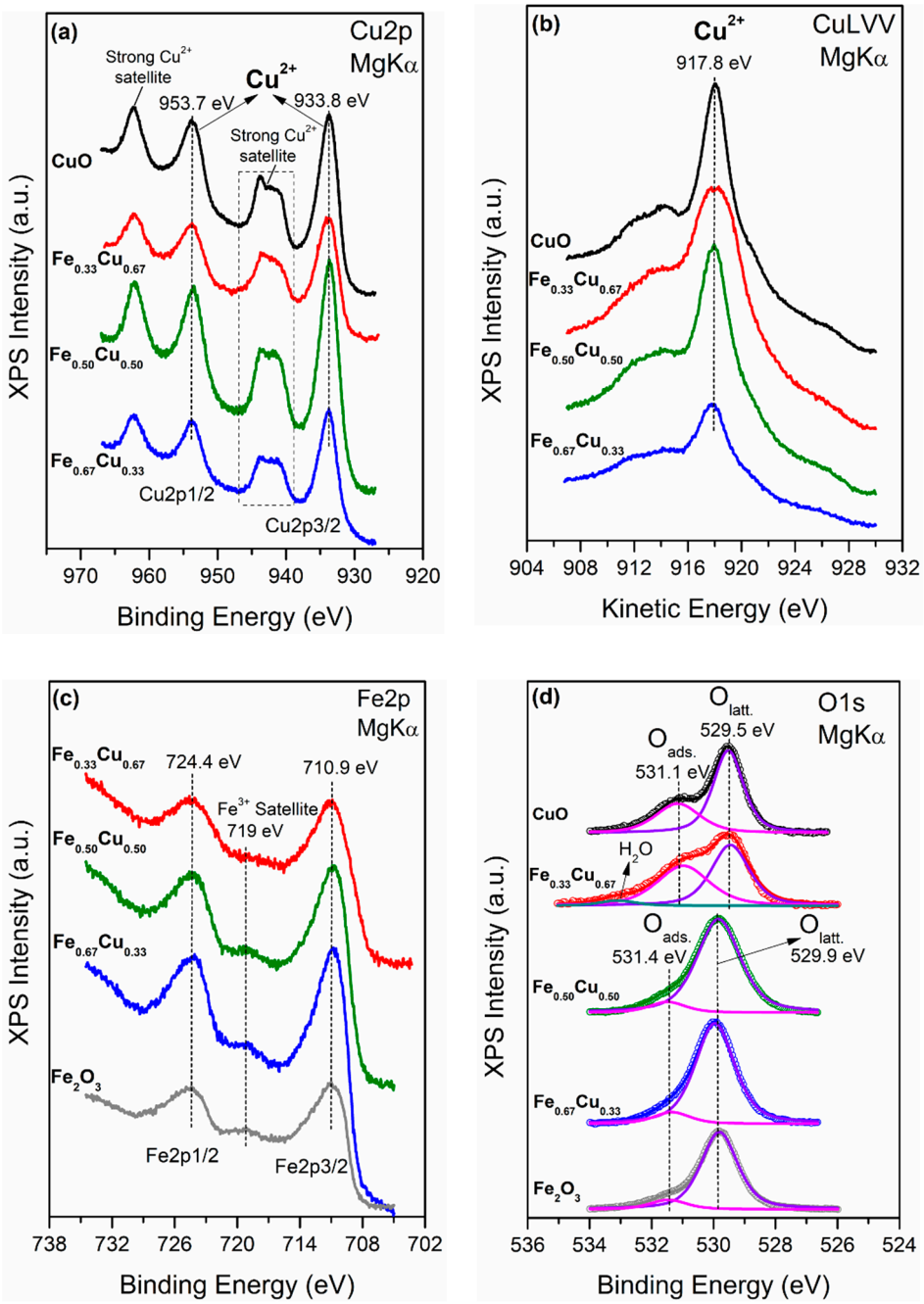


**Figure 4.** (**a**) Cu2p XP spectra, (**b**) CuLVV, (**c**) Fe 2p XP spectra, and (**d**) deconvoluted O1s XP spectra of $Fe_xCu_{1-x}$ catalysts.

The Fe 2p XP spectra of $Fe_xCu_{1-x}$ catalysts are presented in Figure 4c. The core level spectra contain two broad peaks centered at 710.9 eV and 724.4 eV with a spin-orbit

separation at 13.5 eV ascribed to Fe $2p_{3/2}$ and Fe $2p_{1/2}$, respectively. The weak satellite peak positioned at higher binding energy by ~8 eV, at 719 eV, is characteristic of $Fe^{3+}$. $Fe^{2+}$ and $Fe^{3+}$ are mainly distinguished by their satellite features, since $Fe^{2+}$ has a prominent satellite peak at 715 eV whereas, in the case of $Fe^{3+}$, a weak satellite at 719 eV is present [49,50]. In the present case, the only satellite feature was positioned at 719 eV, thus iron was present as $Fe^{3+}$ in the mixed Fe-Cu catalysts.

Figure 4d exhibits the O 1s core level spectra of the studied oxides. The spectra are rather broad, especially in the case of CuO and $Fe_{0.33}Cu_{0.67}$ suggesting the presence of more than one oxygen component; thus, deconvolution was performed. O 1s XP spectra of CuO and $Fe_{0.33}Cu_{0.67}$ include a main peak centered at 529.5 eV attributed to lattice oxygen species with a subsequent shoulder at a higher binding energy of 531.1 eV, which is related to surface hydroxyl species [51]. For the $Fe_{0.33}Cu_{0.67}$ sample, an additional peak at 533 eV can be ascribed to adsorbed water species. For the catalysts with higher iron content, the O 1s spectra were slightly shifted to higher binding energies, that is 529.9 eV for $O^{2-}$ species and 531.4 eV for surface hydroxyl ones. Similar results have been reported for $CuFe_2O_4$ nanoparticles on kaolinite by Dong et al. [52]. The ratio of lattice oxygen with respect to surface hydroxyl species is presented in Table 2. In all samples, lattice oxygen species were the main species observed. The surface composition of $Fe_xCu_{1-x}$ catalysts expressed as the Fe/(Fe + Cu) atomic ratio was determined via XPS measurements and the results are shown in Table 2. It is observed that the surface composition is in agreement with the nominal one for all catalysts. The binding energy values of Cu 2p, Fe 2p, and O 1s are also listed in Table 2.

**Table 2.** Nominal and surface composition determined via XPS measurements, expressed as the atomic ratio Fe/(Fe + Cu), the binding energy values of Cu 2p, Fe 2p, and O 1s peaks and the ratio of lattice oxygen to surface hydroxyl species of $Fe_xCu_{1-x}$ catalysts.

| Catalyst | Fe/(Fe + Cu) Atomic Ratio | | BE (eV) | | | | | |
|---|---|---|---|---|---|---|---|---|
| | Nominal | XPS | Cu 2p | | Fe 2p | | O 1s | $O_{latt.}/O_{ads.}$ |
| | | | $2p_{3/2}$ | $2p_{1/2}$ | $2p_{3/2}$ | $3p_{1/2}$ | | |
| CuO | 0 | 0 | 933.8 | 953.7 | - | | 529.5 | 1.96 |
| $Fe_{0.33}Cu_{0.67}$ | 0.33 | 0.31 | 933.8 | 953.7 | 710.9 | 724.4 | 529.5 | 1.13 |
| $Fe_{0.50}Cu_{0.50}$ | 0.50 | 0.44 | 933.7 | 953.5 | 710.7 | 724.4 | 529.9 | 10.23 |
| $Fe_{0.67}Cu_{0.33}$ | 0.67 | 0.61 | 933.7 | 953.7 | 710.8 | 724.3 | 530.0 | 9.24 |
| $Fe_2O_3$ | 1 | 1 | - | | 711.0 | 724.4 | 529.9 | 8.15 |

### *2.4. Temperature-Programmed Desorption and Surface Reaction of DME over $Fe_xCu_{1-x}$ Catalysts (DME-TPD/TPSR)*

The interaction of DME with $Fe_xCu_{1-x}$ catalysts was investigated employing temperature-programmed desorption experiments (DME-TPD). The catalysts were exposed to a 0.1% DME/He stream at ambient temperature and the obtained DME and $CO_2$ desorption profiles during TPD were expressed per unit surface area as depicted in Figure 5. TPD runs of preadsorbed DME were carried out in the temperature range from 30 to 400 °C with a heating rate of 10 °C $min^{-1}$. For all catalysts, DME desorption profiles (inset of Figure 5) comprised a non-symmetric peak centered at 106–120 °C which was extended up to 200–275 °C. DME desorbs molecularly within this temperature range and taking into account the relatively high temperatures required for the completion of intact DME desorption, it is apparent that DME adsorption on $Fe_xCu_{1-x}$ catalysts is rather strong. The addition of iron on mixed oxide samples led to a gradual increase in molecularly desorbed DME expressed on a surface area basis and to a gradual rise in adsorption strength evidenced by the systematic shift of the DME desorption profiles to higher temperatures. $CO_2$ was also detected during DME-TPD as a consequence of the reaction between irreversibly adsorbed DME and surface oxygen species of the catalysts. $CO_2$ desorption profiles from Fe-Cu mixed oxides were characterized by two peaks, the first one centered at 113–140 °C

and the second one at 237–275 °C, depending on the composition of the catalyst. As the content of iron increases, the low-temperature peak of $CO_2$ is shifted to lower temperatures in contrast to the high-temperature one, which is shifted towards higher temperatures. To understand these observations, we should examine the corresponding profiles of pure CuO and $Fe_2O_3$ oxides. The $CO_2$ desorption profile of $Fe_2O_3$ consisted of a symmetric single peak with a maximum at 313 °C, while in the case of CuO, the corresponding peak was very broad commencing at 150 °C and ending at 300 °C. These results are in accordance with the well-documented inferior catalytic activity of $Fe_2O_3$ in oxidation reactions compared to CuO [42,53]. Hence, for $Fe_{0.67}Cu_{0.33}$, it is apparent that the greater shift of the high-temperature $CO_2$ desorption peak is related to the high content of iron and according to the XRD results, to the formation of $Fe_2O_3$ as a separate phase. Additionally, the low-temperature peak ($T_{max}$ = 113 °C) could be ascribed to highly active sites related to highly dispersed copper-containing species owing to the spinel phase formation. Regarding $Fe_{0.33}Cu_{0.67}$ and $Fe_{0.50}Cu_{0.50}$, the high-temperature peak resembles that of CuO, while the low-temperature peaks are centered at 140 °C and 127 °C, respectively. Furthermore, the TPD results were in compliance with the $H_2$-TPR results, where it was concluded that $Fe_{0.67}Cu_{0.33}$ exhibited the best redox properties among the studied catalysts, indicated by the higher $H_2$ uptake at the low temperature region (<200 °C), demonstrating the higher concentration of easily reducible copper species which is thought to be directly related to the catalytic activity of the samples. In contrast, $H_2$ consumption at higher temperatures is linked to the bulk reduction of the sample which is not related to the catalytic performance.

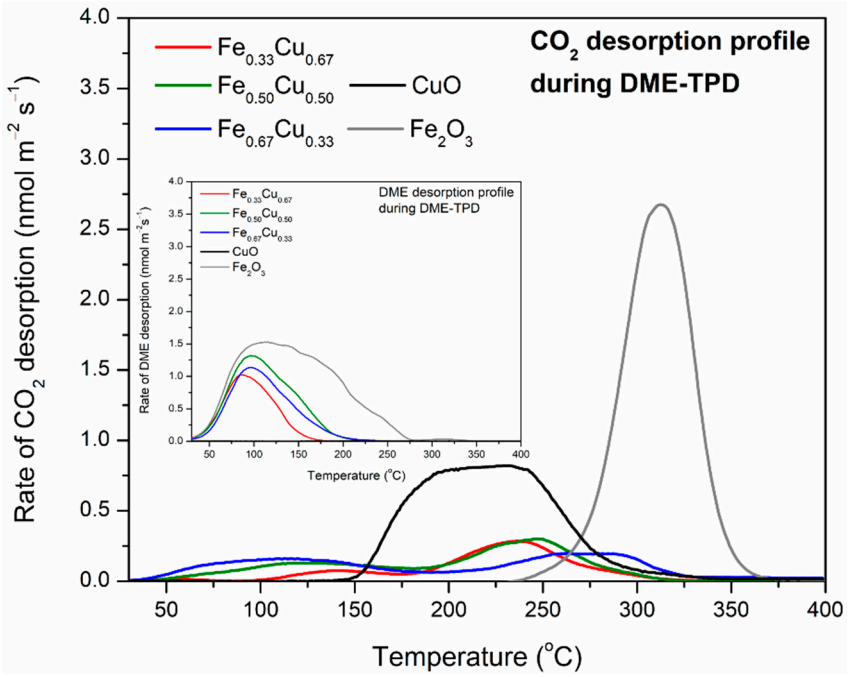


**Figure 5.** TPD profiles of $CO_2$ and DME (inset) after DME adsorption at RT over $Fe_xCu_{1-x}$ catalysts. Conditions: adsorption: 0.1% DME/He, carrier gas: He, flow: 30 $cm^3$ $min^{-1}$.

The amounts of desorbed DME and $CO_2$ after the adsorption of DME at room temperature on $Fe_xCu_{1-x}$ catalysts are listed in Table S1. The quantities of molecularly desorbed DME and $CO_2$ produced over the mixed oxide catalysts are in the range of 7–21 μmol $g_{cat}{}^{-1}$ and 3–7.5 μmol $g_{cat}{}^{-1}$, respectively, which are directly related to the specific surface area of the samples. As expected, the higher the surface area of the sample, the higher the desorbed amount. In order to blot out the effect of surface area on the adsorption capacity of the mixed oxide samples, the desorbed amounts were also expressed on a per unit surface area basis. The amount of produced $CO_2$ during the TPD runs slightly decreased as copper content increased, related to the gradual development of bulk CuO. These findings could provide hints regarding the catalytic activity of $Fe_xCu_{1-x}$ catalysts in DME oxidation

reaction since DME is considered the most appropriate probe to investigate the active sites for the target reaction. Not only the concentration of active sites related to $CO_2$ production, but also the position of the desorption peak at the low-temperature region provide clues regarding the enhanced catalytic activity of $Fe_{0.67}Cu_{0.33}$ catalyst. Focusing on the single oxides, the number density of DME adsorption sites was greater than on the mixed oxides leading to the conclusion that even though pure oxides possess a higher concentration of adsorption sites, they are less active as shown by the position of the desorption peaks towards higher temperatures. DME adsorbs strongly on $Fe_2O_3$ and a comparably elevated temperature is required for its desorption, whereas its oxidation initiates above 250 °C, suggesting a low intrinsic activity for $Fe_2O_3$. In contrast, DME adsorbs irreversibly on CuO since no DME desorption was observed during TPD, while its oxidation through surface oxygen was observed in the temperature range of 150–300 °C, i.e., at temperatures lower than $Fe_2O_3$ but partially higher than mixed oxide catalysts.

DME-TPSR profiles of $Fe_{0.67}Cu_{0.33}$ and $Fe_2O_3$ are shown in Figure S2. The run was carried out under 1% $O_2$/He flow in the temperature range of 30–400 °C. Once again, focusing on the $CO_2$ production profiles acquired, in this case, in the presence of gaseous oxygen, the superiority of $Fe_{0.67}Cu_{0.33}$ catalyst should be pointed out. The existence of the low temperature peak in the mixed oxide sample in opposition to $Fe_2O_3$ marks its higher activity towards DME oxidation. The comparison between TPD and TPSR experiments over $Fe_{0.67}Cu_{0.33}$ and $Fe_2O_3$ catalysts is illustrated in Figure 6. Both samples demonstrate similar TPSR profiles to DME-TPD ones for DME comprising a single peak centered at 95 °C with a shoulder up to 250 °C. The shape of the $CO_2$ production profile during TPSR of $Fe_{0.67}Cu_{0.33}$ catalyst resembled the corresponding one during TPD and consisted of two desorption peaks with slight differences in their intensities. As for $Fe_2O_3$, the symmetrical $CO_2$ desorption peak of TPD was shifted to lower temperatures by ~25 °C while a small shoulder at the lower temperature region (~200 °C) emerged. The shift of the peak maximum is attributed to the facilitated oxidation of DME owing to the fast replenishment of surface oxygen when gaseous oxygen is present during the TPSR run whereas in the case of TPD, the reaction proceeds only with the oxygen provided by the catalyst. Fe–Cu mixed oxide profiles were not significantly altered or shifted to lower temperatures, thus the provided lattice oxygen was easily replenished in this case. Additionally, for $Fe_2O_3$, the amount of produced $CO_2$ increased at the expense of molecularly desorbed DME.

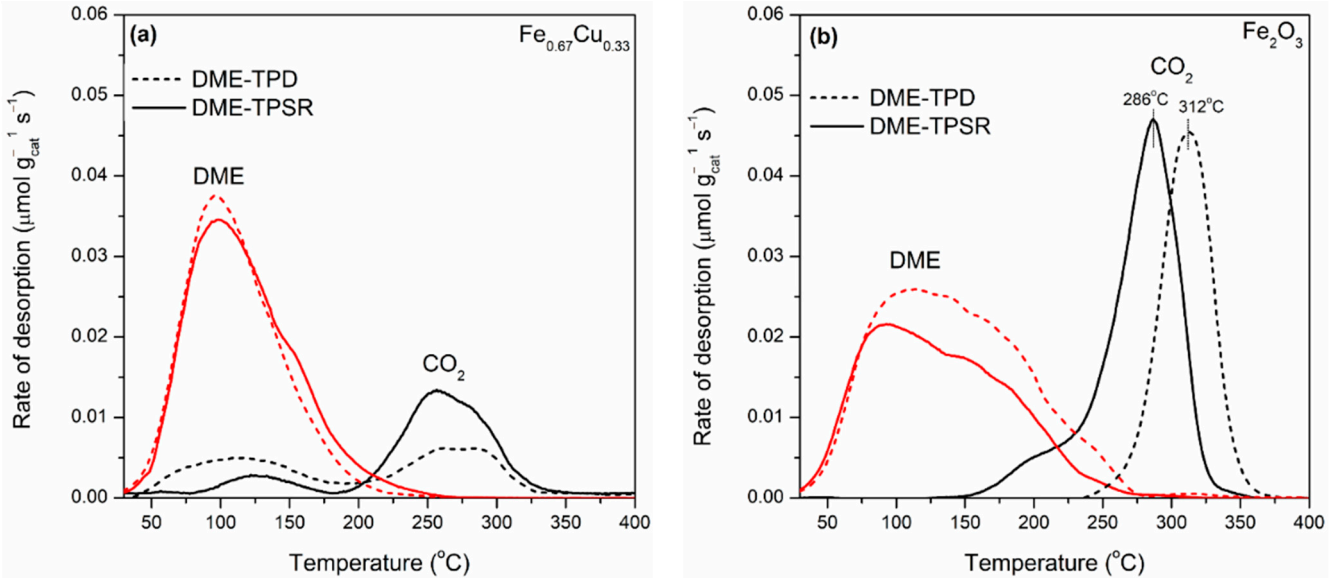


**Figure 6.** Comparison of DME and $CO_2$ desorption profiles resulting from TPD and TPSR experiments over (**a**) $Fe_{0.67}Cu_{0.33}$ and (**b**) $Fe_2O_3$ catalysts. Conditions: adsorption: 0.1% DME/He, carrier gas: He (TPD) or 1% $O_2$/He (TPSR), flow: 30 $cm^3$ $min^{-1}$.

### 2.5. DME Oxidation Activity

$Fe_xCu_{1-x}$ catalysts were evaluated in DME oxidation in the temperature range of 210–380 °C with a W/F ratio of 0.1 g s $cm^{-3}$. The variation of DME conversion with reaction temperature is presented in Figure 7. Pure CuO and $Fe_2O_3$ oxides were also included for comparison. As it can be seen, single oxides exhibited poor catalytic activity towards DME oxidation, where the reaction took place above 240 °C and total DME oxidation was achieved at 380 °C. Both oxides demonstrated similar catalytic activity up to 300 °C while $Fe_2O_3$ prevailed in terms of catalytic performance at higher temperatures achieving almost complete DME conversion at 360 °C ($X_{DME}$ = 98.5%), whereas at the same temperature, DME conversion over CuO was 91%. All the mixed Fe–Cu catalysts were significantly more active than pure oxides, with DME oxidation commencing at 210 °C. The increase in iron content resulted in enhanced catalytic activity. The best-performing catalyst was the $Fe_{0.67}Cu_{0.33}$ attaining a DME conversion of 98% at 300 °C, which is a significant shift of the required temperature for complete DME oxidation by 60 °C compared to pure $Fe_2O_3$. The temperature required for total DME oxidation over $Fe_{0.50}Cu_{0.50}$ catalyst was shifted to a higher temperature by 30 °C compared to the most active catalyst, while $Fe_{0.33}Cu_{0.67}$ was the least active among the mixed Fe–Cu mixed oxides demanding a temperature of 350 °C for complete DME conversion. It should be noted that homogeneous DME oxidation was noticeable at temperatures higher than 320 °C, and DME conversion was 6% at 350 °C in an empty reactor, whereas complete DME conversion was achieved over the $Fe_xCu_{1-x}$ catalysts at that temperature.

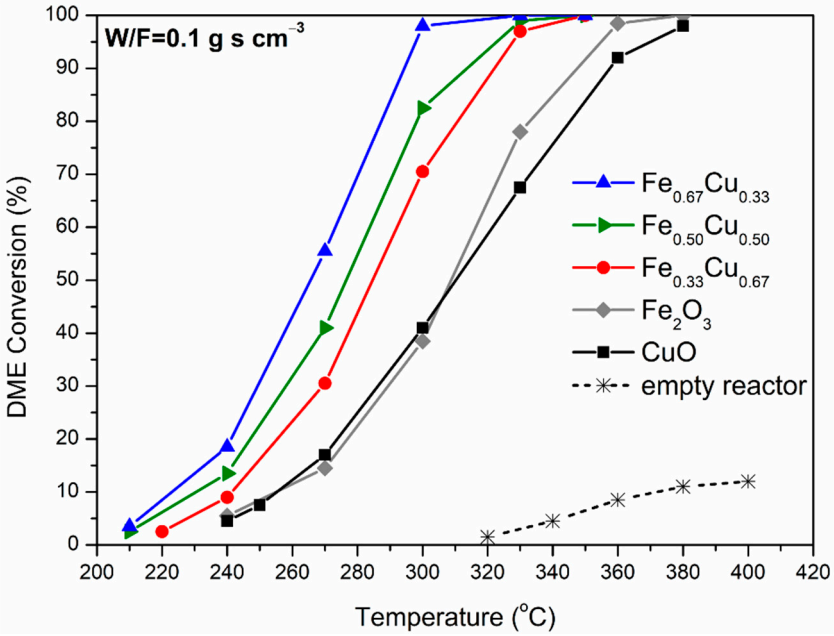


**Figure 7.** DME oxidation activity of $Fe_xCu_{1-x}$ catalysts as a function of the reaction temperature. Homogeneous DME oxidation (empty reactor) is also included. Reaction conditions: 900 ppm DME and 8% $O_2$, W/F = 0.1 g s $cm^{-3}$.

Figure 8 illustrates the DME oxidation rates measured at 240 °C under differential conditions ($X_{DME}$ < 20%) expressed on a unit mass (left axis) and unit surface area (right axis) basis. Focusing on the reaction rates with respect to catalyst weight, the catalytic activity follows the order: $Fe_{0.67}Cu_{0.33}$ (0.078 μmol $g_{cat}^{-1}$ $s^{-1}$) > $Fe_{0.50}Cu_{0.50}$ (0.055 μmol $g_{cat}^{-1}$ $s^{-1}$) > $Fe_{0.33}Cu_{0.67}$ (0.037 μmol $g_{cat}^{-1}$ $s^{-1}$) > $Fe_2O_3$ (0.023 μmol $g_{cat}^{-1}$ $s^{-1}$) > CuO (0.018 μmol $g_{cat}^{-1}$ $s^{-1}$). As previously mentioned, the DME oxidation rate, on a mass basis, increased with increase in iron loading for $Fe_xCu_{1-x}$ catalysts reaching an optimum value for $Fe_{0.67}Cu_{0.33}$ catalyst, which is approximately 3.5–4 times higher than those of pure oxides. The enhanced catalytic activity of $Fe_{0.67}Cu_{0.33}$ is directly related to its higher

specific surface area compared to the other catalysts, but this is not the only factor influencing catalytic activity since the $Fe_{0.50}Cu_{0.50}$ sample has similar specific surface area but significantly inferior activity. The reducibility of the samples is another factor influencing catalytic activity since the oxidation reactions are linked to the catalyst redox properties. Indeed, the results collected from $H_2$-TPR are in complete agreement with the catalytic activity tests. It was demonstrated that the concentration of easily reducible, highly dispersed copper-containing species was higher over $Fe_{0.67}Cu_{0.33}$ owing to the higher content of the cuprospinel phase and the lower content of the bulk CuO phase compared to the other Fe-Cu mixed oxides, as shown by the XRD measurements. DME-TPD/TPSR has also shown that $Fe_{0.67}Cu_{0.33}$ contains more sites able to oxidize preadsorbed DME to $CO_2$ at low temperatures than all other catalysts.

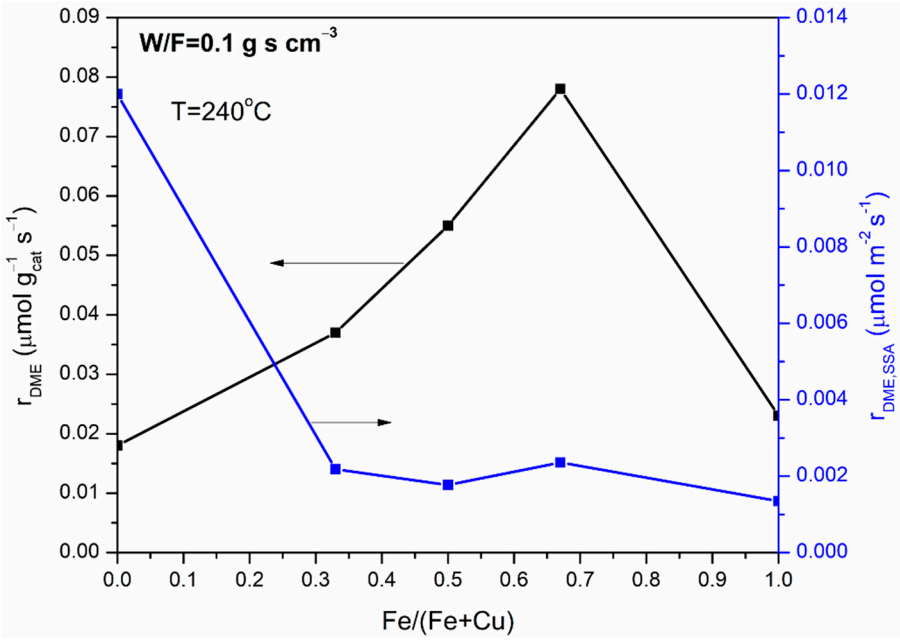


**Figure 8.** Variation of reaction rates expressed per catalyst weight (in μmol $g_{cat}^{-1}$ $s^{-1}$, left axis) and specific reaction rates (in μmol $m^{-2}$ $s^{-1}$, right axis) of DME oxidation with the Fe/(Fe+Cu) molar ratio. Reaction conditions: 900 ppm DME and 8% $O_2$, reaction temperature = 240 °C, W/F = 0.1 g s $cm^{-3}$.

The DME oxidation rates per unit surface area of $Fe_xCu_{1-x}$ (specific rates, μmol $m^{-2}$ $s^{-1}$) are also shown in Figure 8 (right axis). The specific rates of pure CuO and $Fe_2O_3$ oxides are also included and the ranking is CuO (12 nmol $m^{-2}$ $s^{-1}$) >> $Fe_{0.67}Cu_{0.33}$ (2.4 nmol $m^{-2}$ $s^{-1}$) > $Fe_{0.33}Cu_{0.67}$ (2.2 nmol $m^{-2}$ $s^{-1}$) > $Fe_{0.50}Cu_{0.50}$ (1.8 nmol $m^{-2}$ $s^{-1}$) > $Fe_2O_3$ (1.4 nmol $m^{-2}$ $s^{-1}$). CuO exhibits the highest intrinsic activity under differential conditions in DME oxidation even though it achieves complete DME conversion at higher temperatures compared to $Fe_xCu_{1-x}$ mixed oxides. Nevertheless, it should be noted that the significant difference in specific surface areas between CuO and Fe–Cu mixed oxides may result in misleading conclusions and therefore a CuO sample with similar specific surface area would be more appropriate. However, the current synthetic method does not permit the development of higher surface areas regarding CuO and changing the preparation method might alter other features as well, which in turn would not allow the direct comparison of the catalysts. The specific rate of $Fe_{0.67}Cu_{0.33}$ is slightly higher than the other mixed oxides and approximately double compared to $Fe_2O_3$. As demonstrated by the TPD experiments, iron–copper mixed oxides possess sites of higher activity (shown by the low-temperature peak in $CO_2$ production profiles) than single oxides; nonetheless, the concentration of DME adsorption sites diminishes in the mixed oxides compared to the single ones. Hence, one could assume that the lower intrinsic activity of the mixed oxides is related to the lower number density of adsorption sites compared to CuO. As for $Fe_2O_3$, indeed, it has the highest concentration of DME adsorption sites, which, however, are notably less active in

DME oxidation leading to inferior specific activity. In any case, the lower specific activity of the $Fe_xCu_{1-x}$ catalysts is overcompensated by their larger specific surface areas leading to notably enhanced catalytic activity overall.

The stability of the $Fe_{0.67}Cu_{0.33}$ catalyst was assessed in DME oxidation at 300 °C for more than 50 h. The catalyst performance as a function of time-on-stream is shown in Figure S3. The catalyst demonstrates exceptional stability retaining its initial activity during the tested period ($X_{DME}$ = 97–98%).

The presence of water vapor in the feed stream is usual in most practical applications where catalytic oxidation of VOC is employed, including the emission control systems in various industrial plants. Hence, it would be of interest to examine the impact of water presence on the catalytic performance of $Fe_xCu_{1-x}$ catalysts in DME oxidation. The influence of $H_2O$ vapor (3% $H_2O$) in the reactant feed was also investigated and the catalytic tests took place in the temperature range of 240–420 °C with W/F = 0.1 g s $cm^{-3}$ and the corresponding conversion curves are shown in Figure 9. The presence of 3% $H_2O$ vapor in the feed led to a decrease in the catalytic activity of all samples shifting the required temperature for complete DME conversion to a higher temperature by ~30–40 °C. However, there was no change regarding the catalyst ranking, with $Fe_{0.67}Cu_{0.33}$ remaining as the best-performing catalyst in DME oxidation even in the presence of water vapor. DME oxidation over $Fe_{0.67}Cu_{0.33}$ initiated at 240 °C while a temperature of 300 °C was required for the complete conversion of DME to $CO_2$. The oxidation rates and specific rates measured at 270 °C in the presence of water vapor as a function of Fe/(Fe + Cu) molar ratio are presented in Figure S4. The trends observed in terms of reaction rates and intrinsic activity in the presence of $H_2O$ vapor are similar to those previously mentioned in its absence. It is well established that $H_2O$ titrates the active sites of the transition metal oxides leading to a decrease in catalytic activity, which is also the case in DME oxidation [19,37,54].

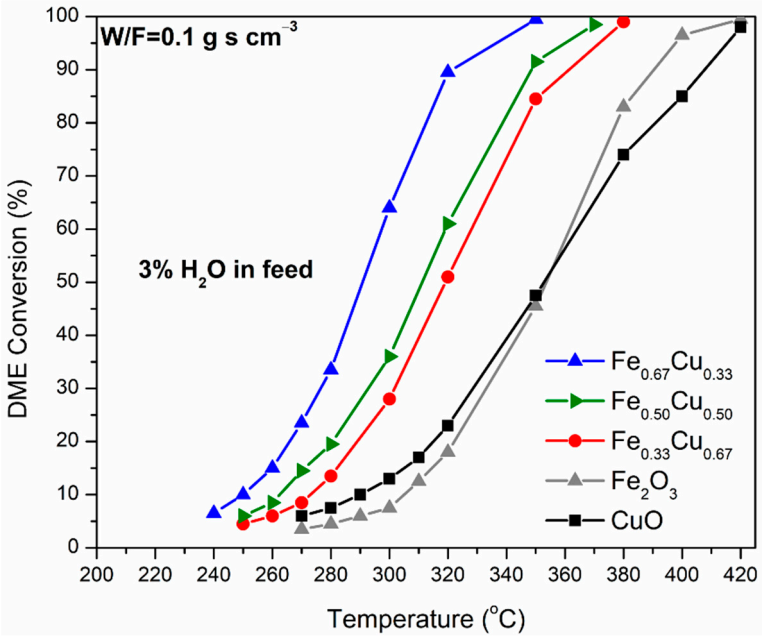


**Figure 9.** Conversion curves of DME oxidation in the presence of 3% $H_2O$ vapor over $Fe_xCu_{1-x}$ catalysts. Reaction conditions: 900 ppm DME, 8% $O_2$, and 3% $H_2O$, W/F = 0.1 g s $cm^{-3}$.

## 3. Materials and Methods

### *3.1. Catalysts Synthesis*

$Fe_xCu_{1-x}$ mixed oxide catalysts were synthesized with molar ratios Fe/(Fe + Cu) = 0.33, 0.50, 0.67 employing the citrate complexation method reported by Duran et al. [55]. $Fe(NO_3)_3 \cdot 9\ H_2O$ (Alfa Aesar, Kandel, Germany, 8.0–101.0%), $Cu(NO_3)_2 \cdot 2.5\ H_2O$ (Sigma Aldrich, St. Louis, MO, USA, 98%), and citric acid monohydrate (Penta, Berlin, Germany, 99.5%) were used as starting reagents. The molar ratio of citric acid to nitrate salts was

fixed at 1.1. The aqueous solutions of metal nitrates were prepared separately and then were added to the citric acid solution followed by vigorous stirring for 15 min at room temperature. The resulting solution was evaporated under vacuum at 50 °C until a viscous liquid was formed followed by drying under static air at 120 °C overnight. The resulting spongy citrate precursors were crushed and heated to 500 °C under static air with a heating rate of 2 °C $min^{-1}$ and remained at that temperature for 2 h. Catalysts are denoted as $Fe_xCu_{1-x}$, where x is the Fe/(Fe + Cu) molar ratio of the as-prepared catalysts. CuO and $Fe_2O_3$ pure oxides were also prepared following the same procedure for comparison.

### *3.2. Catalyst Characterization*

The textural properties of the fresh samples were determined from the adsorption–desorption isotherms of nitrogen at −196 °C, recorded with a Micromeritics TriStar 3000 apparatus. Prior to the experiments, the samples were degassed at 300 °C in vacuum for 1 h. $N_2$ adsorption isotherms were measured at $0.01 < P/P_0 < 0.99$. The adsorption data were then used to determine BET surface area ($0.06 < P/P_0 < 0.20$), total pore volume at $P/P_0 \approx 0.99$, and pore size distribution (PSD) using the Barret–Joyner–Halenda (BJH) model. The pore size distribution (PSD) curves were calculated by applying the BJH method to the adsorption branches of the $N_2$ isotherms.

The crystalline structure of the catalysts was investigated by means of an X-ray powder diffractometer (Bruker D8 Advance) operated at 40 mA and 40 kV by employing a Ni-filtered Cu Ka radiation (λ = 1.5418 Å). XRD patterns were obtained in the range of $20° < 2\theta < 100°$ with a scan step of 0.02° and a scan speed of 5 s/step. Rietveld refinement was employed for the obtained XRD diffractograms using the Maud software according to Lutterotti et al. [56].

Temperature-programmed reduction ($H_2$-TPR) experiments were performed under a flow of a 3% $H_2$/He (30 $cm^3$ $min^{-1}$) from room temperature to 700 °C with a heating rate of 10 °C $min^{-1}$. Prior to TPR, a powdered sample of 25 mg was treated under air at 500 °C for 15 min. A mass spectrometer (Omnistar GSD 320/Pfeiffer Vacuum) was used for on-line monitoring of TPR effluent gas.

Surface chemistry analysis of the samples was conducted by means of X-ray photoelectron spectroscopy (XPS) in a UHV chamber (5 × 10−10 mbar) equipped with a SPECS Phoibos 100–1D-DLD hemispherical electron analyzer and a non-monochromatized dual-anode Mg/Al X-ray source. The XP spectra were recorded using MgKa at 1253.6 eV photon energy and an analyzer pass energy of 10 eV. The diameter of the analyzed area spot was 7 × 15 mm. For the spectra collection and fitting, the commercial software SpecsLab Prodigy (Specs GmbH, Berlin) was used. The binding energies were calculated with reference to the energy of C 1s peak of contaminant carbon at 284.6 eV. All samples were in powder form and prior to XPS measurements, they were pressed into a pellet.

DME temperature-programmed desorption (DME-TPD) and DME temperature-programmed surface reaction (DME-TPSR) experiments were conducted under atmospheric pressure in a fixed-bed reactor system with two independent gas lines equipped with mass flow controllers (Aera GmbH, Kirchheim, Germany), while a mass spectrometer (Omnistar/Pfeiffer Vacuum, Asslar, Germany) was used for on-line monitoring of effluent gases. Prior to each DME adsorption experiment, the sample (its weight varied in order to have 3.3 $m^2$ in the reactor, 90 μm < d < 180 μm) was thermally pretreated under 20% $O_2$/He flow (30 $cm^3$ $min^{-1}$) up to 500 °C with a linear heating rate of 10 °C $min^{-1}$ for 15 min, followed by cooling down to room temperature under He flow. DME adsorption took place at room temperature under a flow of 0.1% DME/He. The feed also contained Ar (2 $cm^3$ $min^{-1}$) as inert tracer. After completion of adsorption, indicated by stable signals in the mass spectrometer, the reactor was purged with He until all signals met their baselines. Then, the TPD run was initiated under He flow of 30 $cm^3$ $min^{-1}$ from 30 to 400 °C with a heating rate of 10 °C $min^{-1}$. DME-TPSR runs were performed under 1% $O_2$/He flow.

### *3.3. Catalyst Evaluation Tests*

The catalysts were evaluated in dimethyl ether oxidation in the absence and presence of 3% $H_2O$ vapor and the tests were carried out in a conventional quartz flow reactor with fixed bed at atmospheric pressure and reaction temperatures in the range of 210–420 °C. Prior to all catalytic tests, the samples were heated under 20 vol.% $O_2$/He mixture at 300 °C for 1 h. All runs were performed using 0.1 g of catalyst (crushed and sieved to particle size 90 < dp < 180 μm) under a reactant flow rate of 60 $cm^3$ $min^{-1}$ (W/F = 0.1 g s $cm^{-3}$). A blank test without catalyst was also performed under the same conditions. The gas mixture contained: 900 ppm DME (≥99.9%, Sigma Aldrich), 8% $O_2$ (20% $O_2$/He, Linde Hellas), and He (99.999%, Linde Hellas) balance. $H_2O$ vapor was introduced by flowing gas mixture through a saturator at room temperature. The reactant and product composition were analyzed online by a gas chromatograph (Shimadzu GC-14B) equipped with a flame ionization detector (FID) and a thermal conductivity detector (TCD). The employed chromatographic columns were 0.19% Picric acid/Graphpac-CC 80/100, $7' \times 1/8'' \times 0.085''$/SS (for DME analysis) and 45/60 Carboxen 1000, $5' \times 1/8''$/SS (for $O_2$ and $CO_2$ analysis).

The conversion (X) of DME was calculated using the following equation taking into account that $CO_2$ was the only product of the reaction:

$$X_{DME}(\%) = \frac{C_{DME}^{in} - C_{DME}^{out}}{C_{DME}^{in}} \times 100 \quad (1)$$

where $C_{DME}^{in}$ and $C_{DME}^{out}$ are the feed and outlet concentration of DME.

For the calculation of the reaction rates per unit catalyst weight ($r_{DME}$, in μmol $g_{cat}{}^{-1}$ $s^{-1}$) the following equation was used:

$$r_{DME} = \frac{F_{DME}\, X_{DME}}{w} \quad (2)$$

where $F_{DME}$ is the molar flow of DME (in μmol $s^{-1}$), $X_{DME}$ is the conversion of DME to $CO_2$, and w is the catalyst weight (in g).

For the calculation of the specific reaction rates ($r_{DME,SSA}$, in μmol $m^{-2}$ $s^{-1}$), the following equation was used:

$$r_{DME,SSA} = \frac{r_{DME}}{SSA} \quad (3)$$

where $r_{DME}$ is the reaction rate on a unit catalyst weight of DME oxidation (in μmol $g_{cat}{}^{-1}$ $s^{-1}$) and SSA is the specific surface area of the catalysts (in $m^2$ $g_{cat}{}^{-1}$).

Catalytic experiments were repeated three times with different samples for the optimal catalyst and the deviation in measurements of reaction rate was less than 5% from the mean value.

## 4. Conclusions

$Fe_xCu_{1-x}$ mixed oxide catalysts were prepared employing the citrate complexation method and were evaluated in dimethyl ether (DME) oxidation. $Fe_{0.67}Cu_{0.33}$ was the best-performing catalyst among the examined mixed Fe-Cu oxides attaining approximately a 4-fold higher oxidation rate compared to pure oxides. The enhanced catalytic performance was attributed to the higher specific surface area of the catalyst and its enhanced redox properties, as suggested by the $H_2$-TPR experiments. The formation of highly dispersed thus easily reducible $Cu^{2+}$ species was induced by the formation of the cuprospinel phase in combination with the diminution of bulk CuO. DME-TPD/TPSR experiments provided further evidence of the improved catalytic performance of the $Fe_{0.67}Cu_{0.33}$ exhibiting the most active surface sites among the studied catalysts, as demonstrated by the $CO_2$ production profiles during TPD/TPSR. Pure CuO demonstrated the highest specific activity even though a significantly higher temperature is required for complete DME conversion over CuO compared to $Fe_xCu_{1-x}$ mixed oxides. The combination of the two metal oxides results in a decrease of DME adsorption sites in comparison to CuO, hence, it is possible that the

lower specific activity of the mixed oxides is related to their lower concentration of adsorption sites. Even so, the lower specific activity of the $Fe_xCu_{1-x}$ catalysts is overcompensated by their larger specific surface areas leading to notably enhanced overall catalytic activity. The presence of water vapor had an inhibiting effect on the catalytic activity of the samples shifting the required temperature for total DME oxidation towards higher temperatures.

**Supplementary Materials:** The following supporting information can be downloaded at: https://www.mdpi.com/article/10.3390/catal12060604/s1, Figure S1: Rietveld refined XRD diffractograms of $Fe_xCu_{1-x}$ catalysts; Figure S2: DME-TPSR profiles of $Fe_{0.67}Cu_{.33}$ and $Fe_2O_3$ catalysts; Figure S3: Stability test of $Fe_{0.67}Cu_{0.33}$ catalyst; Figure S4: Variation of DME oxidation rates in the presence of $H_2O$ vapor expressed per catalyst weight (in μmol $g_{cat}{}^{-1}$ $s^{-1}$, left axis) and specific reaction rates (in μmol $m^{-2}$ $s^{-1}$, right axis) with the Fe/(Fe + Cu) molar ratio; Table S1: Amounts of desorbed DME and $CO_2$ expressed per catalyst weight and surface area over $Fe_xCu_{1-x}$ catalysts ($0.33 \leq x \leq 0.67$) and single $Fe_2O_3$ and CuO oxides during DME-TPD and DME-TPSR experiments; Table S2: Summary of the literature in DME oxidation over (mixed) oxide catalysts.

**Author Contributions:** M.S.: methodology; validation; formal analysis; investigation; data curation; writing—original draft preparation. T.I.: conceptualization; methodology; validation; formal analysis; investigation; resources; writing—review and editing; supervision; project administration; funding acquisition. All authors have read and agreed to the published version of the manuscript.

**Funding:** This research has been co-financed by European Union and Greek national funds through the Operational Program Competitiveness, Entrepreneurship, and Innovation, under the call RESEARCH–CREATE–INNOVATE (project code: T1EDK-01704).

**Acknowledgments:** The authors would like to thank Yiannis Georgiou for his assistance with the Rietveld refinement of the XRD diffractograms.

**Conflicts of Interest:** The authors declare no conflict of interest.

## References

1. Semelsberger, T.A.; Ott, K.C.; Borup, R.L.; Greene, H.L. Generating Hydrogen-Rich Fuel-Cell Feeds from Dimethyl Ether (DME) Using Cu/Zn Supported on Various Solid-Acid Substrates. *Appl. Catal. A Gen.* **2006**, *309*, 210–223. [CrossRef]
2. Han, D.; Yin, H.; Qian, E.; Ye, L.; Liu, D. Pyrolysis and Catalysis of Dimethyl Ether in a Flow Reactor. *Fuel* **2020**, *263*, 116700. [CrossRef]
3. Arcoumanis, C.; Bae, C.; Crookes, R.; Kinoshita, E. The Potential of Di-Methyl Ether (DME) as an Alternative Fuel for Compression-Ignition Engines: A Review. *Fuel* **2008**, *87*, 1014–1030. [CrossRef]
4. Mihai, O.; Fathali, A.; Auvray, X.; Olsson, L. DME, Propane and CO: The Oxidation, Steam Reforming and WGS over $Pt/Al_2O_3$. The Effect of Aging and Presence of Water. *Appl. Catal. B Environ.* **2014**, *160–161*, 480–491. [CrossRef]
5. Cheng, G.; Yu, L.; He, B.; Sun, M.; Zhang, B.; Ye, W.; Lan, B. Catalytic Combustion of Dimethyl Ether over α-$MnO_2$ Nanostructures with Different Morphologies. *Appl. Surf. Sci.* **2017**, *409*, 223–231. [CrossRef]
6. Sun, M.; Yu, L.; Ye, F.; Diao, G.; Yu, Q.; Hao, Z.; Zheng, Y.; Yuan, L. Transition Metal Doped Cryptomelane-Type Manganese Oxide for Low-Temperature Catalytic Combustion of Dimethyl Ether. *Chem. Eng. J.* **2013**, *220*, 320–327. [CrossRef]
7. Tabakova, T.; Kolentsova, E.; Dimitrov, D.; Ivanov, K.; Manzoli, M.; Venezia, A.M.; Karakirova, Y.; Petrova, P.; Nihtianova, D.; Avdeev, G. CO and VOCs Catalytic Oxidation Over Alumina Supported Cu–Mn Catalysts: Effect of Au or Ag Deposition. *Top. Catal.* **2017**, *60*, 110–122. [CrossRef]
8. Huang, H.; Xu, Y.; Feng, Q.; Leung, D.Y.C. Low Temperature Catalytic Oxidation of Volatile Organic Compounds: A Review. *Catal. Sci. Technol.* **2015**, *5*, 2649–2669. [CrossRef]
9. Santos, V.P.; Carabineiro, S.A.C.; Tavares, P.B.; Pereira, M.F.R.; Órfão, J.J.M.; Figueiredo, J.L. Oxidation of CO, Ethanol and Toluene over $TiO_2$ Supported Noble Metal Catalysts. *Appl. Catal. B Environ.* **2010**, *99*, 198–205. [CrossRef]
10. Scirè, S.; Liotta, L.F. Supported Gold Catalysts for the Total Oxidation of Volatile Organic Compounds. *Appl. Catal. B Environ.* **2012**, *125*, 222–246. [CrossRef]
11. Papaefthimiou, P.; Ioannides, T.; Verykios, X.E. Performance of Doped $Pt/TiO_2$ ($W^{6+}$) Catalysts for Combustion of Volatile Organic Compounds (VOCs). *Appl. Catal. B Environ.* **1998**, *15*, 75–92. [CrossRef]
12. Liotta, L.F. Catalytic Oxidation of Volatile Organic Compounds on Supported Noble Metals. *Appl. Catal. B Environ.* **2010**, *100*, 403–412. [CrossRef]
13. Ishikawa, A.; Iglesia, E. Bifunctional Pathways Mediated by Pt Clusters and $Al_2O_3$ in the Catalytic Combustion of Dimethyl Ether. *Chem. Commun.* **2007**, *28*, 2992–2993. [CrossRef]
14. Solymosi, F.; Cserényi, J.; Ovári, L. A comparative study of the complete oxidation of dimethyl ether on supported group VIII metals. *Catal. Lett.* **1997**, *44*, 89–93. [CrossRef]

15. Idakiev, V.; Dimitrov, D.; Tabakova, T.; Ivanov, K.; Yuan, Z.-Y.; Su, B.-L. Catalytic Abatement of CO and Volatile Organic Compounds in Waste Gases by Gold Catalysts Supported on Ceria-Modified Mesoporous Titania and Zirconia. *Chin. J. Catal.* **2015**, *36*, 579–587. [CrossRef]
16. Xie, X.; Li, Y.; Liu, Z.-Q.; Haruta, M.; Shen, W. Low-Temperature Oxidation of CO Catalysed by $Co_3O_4$ Nanorods. *Nature* **2009**, *458*, 746–749. [CrossRef]
17. Krämer, M.; Schmidt, T.; Stöwe, K.; Maier, W.F. Structural and Catalytic Aspects of Sol–Gel Derived Copper Manganese Oxides as Low-Temperature CO Oxidation Catalyst. *Appl. Catal. A Gen.* **2006**, *302*, 257–263. [CrossRef]
18. Chen, X.; Carabineiro, S.A.C.; Bastos, S.S.T.; Tavares, P.B.; Órfão, J.J.M.; Pereira, M.F.R.; Figueiredo, J.L. Exotemplated Copper, Cobalt, Iron, Lanthanum and Nickel Oxides for Catalytic Oxidation of Ethyl Acetate. *J. Environ. Chem. Eng.* **2013**, *1*, 795–804. [CrossRef]
19. Delimaris, D.; Ioannides, T. VOC Oxidation over CuO–$CeO_2$ Catalysts Prepared by a Combustion Method. *Appl. Catal. B Environ.* **2009**, *89*, 295–302. [CrossRef]
20. Soltan, W.B.; Sun, J.; Wang, W.; Song, Z.; Zhao, X.; Mao, Y.; Zhang, Z. Discovering the Key Role of $MnO_2$ and $CeO_2$ Particles in the $Fe_2O_3$ Catalysts for Enhancing the Catalytic Oxidation of VOC: Synergistic Effect of the Lattice Oxygen Species and Surface-Adsorbed Oxygen. *Sci. Total Environ.* **2022**, *819*, 152844. [CrossRef]
21. Rodriguez, J.A.; Jirsak, T.; Pérez, M.; Chaturvedi, S.; Kuhn, M.; González, L.; Maiti, A. Studies on the Behavior of Mixed-Metal Oxides and Desulfurization: Reaction of $H_2S$ and $SO_2$ with $Cr_2O_3$ (0001), MgO(100), and $Cr_xMg_{1-x}O$(100). *J. Am. Chem. Soc.* **2000**, *122*, 12362–12370. [CrossRef]
22. Liotta, L.F.; Ousmane, M.; Di Carlo, G.; Pantaleo, G.; Deganello, G.; Boreave, A.; Giroir-Fendler, A. Catalytic Removal of Toluene over $Co_3O_4$–$CeO_2$ Mixed Oxide Catalysts: Comparison with Pt/$Al_2O_3$. *Catal. Lett.* **2009**, *127*, 270–276. [CrossRef]
23. Shah, P.M.; Burnett, J.W.H.; Morgan, D.J.; Davies, T.E.; Taylor, S.H. Ceria–Zirconia Mixed Metal Oxides Prepared via Mechanochemical Grinding of Carbonates for the Total Oxidation of Propane and Naphthalene. *Catalysts* **2019**, *9*, 475. [CrossRef]
24. Jirátová, K.; Kovanda, F.; Ludvíková, J.; Balabánová, J.; Klempa, J. Total Oxidation of Ethanol over Layered Double Hydroxide-Related Mixed Oxide Catalysts: Effect of Cation Composition. *Catal. Today* **2016**, *277*, 61–67. [CrossRef]
25. Neha; Prasad, R.; Singh, S.V. Catalytic Abatement of CO, HCs and Soot Emissions over Spinel-Based Catalysts from Diesel Engines: An Overview. *J. Environ. Chem. Eng.* **2020**, *8*, 103627. [CrossRef]
26. Davari, E.; Ivey, D.G. Bifunctional Electrocatalysts for Zn–Air Batteries. *Sustain. Energy Fuels* **2018**, *2*, 39–67. [CrossRef]
27. Manos, D.; Miserli, K.; Konstantinou, I. Perovskite and Spinel Catalysts for Sulfate Radical-Based Advanced Oxidation of Organic Pollutants in Water and Wastewater Systems. *Catalysts* **2020**, *10*, 1299. [CrossRef]
28. Zhao, Q.; Yan, Z.; Chen, C.; Chen, J. Spinels: Controlled Preparation, Oxygen Reduction/Evolution Reaction Application, and Beyond. *Chem. Rev.* **2017**, *117*, 10121–10211. [CrossRef]
29. Ren, L.; Zhong, Y.; Xu, J.; Chen, J.; Zou, T.; Liao, X.-L.; Chen, Z.-F.; Yu, L. Nano $Fe_{3-x}Cu_xO_4$ as the Heterogeneous Catalyst in an Advanced Oxidation Process for Excellent Peroxymonosulfate Activation toward Climbazole Degradation. *Chem. Eng. J.* **2022**, *439*, 135553. [CrossRef]
30. Yan, K.; Wu, X.; An, X.; Xie, X. Facile Synthesis and Catalytic Property of Spinel Ferrites by a Template Method. *J. Alloy Compd.* **2013**, *552*, 405–408. [CrossRef]
31. Ren, Y.; Lin, L.; Ma, J.; Yang, J.; Feng, J.; Fan, Z. Sulfate Radicals Induced from Peroxymonosulfate by Magnetic Ferrospinel $MFe_2O_4$ (M = Co, Cu, Mn, and Zn) as Heterogeneous Catalysts in the Water. *Appl. Catal. B Environ.* **2015**, *165*, 572–578. [CrossRef]
32. Manikandan, A.; Sridhar, R.; Arul Antony, S.; Ramakrishna, S. A Simple Aloe Vera Plant-Extracted Microwave and Conventional Combustion Synthesis: Morphological, Optical, Magnetic and Catalytic Properties of $CoFe_2O_4$ Nanostructures. *J. Mol. Struct.* **2014**, *1076*, 188–200. [CrossRef]
33. Liu, P.; He, H.; Wei, G.; Liang, X.; Qi, F.; Tan, F.; Tan, W.; Zhu, J.; Zhu, R. Effect of Mn Substitution on the Promoted Formaldehyde Oxidation over Spinel Ferrite: Catalyst Characterization, Performance and Reaction Mechanism. *Appl. Catal. B Environ.* **2016**, *182*, 476–484. [CrossRef]
34. Tian, Z.-Y.; Mountapmbeme Kouotou, P.; El Kasmi, A.; Tchoua Ngamou, P.H.; Kohse-Höinghaus, K.; Vieker, H.; Beyer, A.; Gölzhäuser, A. Low-Temperature Deep Oxidation of Olefins and DME over Cobalt Ferrite. *Proc. Combust. Inst.* **2015**, *35*, 2207–2214. [CrossRef]
35. Djinović, P.; Ristić, A.; Žumbar, T.; Dasireddy, V.D.B.C.; Rangus, M.; Dražić, G.; Popova, M.; Likozar, B.; Zabukovec Logar, N.; Novak Tušar, N. Synergistic Effect of CuO Nanocrystals and Cu-Oxo-Fe Clusters on Silica Support in Promotion of Total Catalytic Oxidation of Toluene as a Model Volatile Organic Air Pollutant. *Appl. Catal. B Environ.* **2020**, *268*, 118749. [CrossRef]
36. Tu, Y.-J.; Chang, C.-K.; You, C.-F. Combustion of Isopropyl Alcohol Using a Green Manufactured $CuFe_2O_4$. *J. Hazard. Mater.* **2012**, *229–230*, 258–264. [CrossRef]
37. Amini, E.; Rezaei, M. Preparation of Mesoporous Fe-Cu Mixed Metal Oxide Nanopowder as Active and Stable Catalyst for Low-Temperature CO Oxidation. *Chin. J. Catal.* **2015**, *36*, 1711–1718. [CrossRef]
38. Popescu, I.; Boudjemaa, A.; Helaili, N.; Bessekhouad, Y.; Tudorache, M.; Bachari, K.; Marcu, I.-C. Study of the Electrical and Catalytic Properties of Spinels with $CuFe_{2-x}Mn_xO_4$ Composition (X = 0, 0.4, 0.8, 1.6 and 2). *Appl. Catal. A Gen.* **2015**, *504*, 29–36. [CrossRef]

39. Liu, H.; Liu, L.; Wei, L.; Chu, B.; Qin, Z.; Jin, G.; Tong, Z.; Dong, L.; Li, B. Preparation of Three-Dimensionally Ordered Macroporous $MFe_2O_4$ (M = Co, Ni, Cu) Spinel Catalyst and Its Simultaneous Catalytic Application in CO Oxidation and NO + CO Reaction. *Fuel* **2020**, *272*, 117738. [CrossRef]
40. Rezlescu, N.; Rezlescu, E.; Popa, P.D.; Popovici, E.; Doroftei, C.; Ignat, M. Preparation and Characterization of Spinel-Type $MeFe_2O_4$ (Me = Cu, Cd, Ni and Zn) for Catalyst Applications. *Mater. Chem. Phys.* **2013**, *137*, 922–927. [CrossRef]
41. Tsoncheva, T.; Manova, E.; Velinov, N.; Paneva, D.; Popova, M.; Kunev, B.; Tenchev, K.; Mitov, I. Thermally Synthesized Nanosized Copper Ferrites as Catalysts for Environment Protection. *Catal. Commun.* **2010**, *12*, 105–109. [CrossRef]
42. Yeste, M.P.; Vidal, H.; García-Cabeza, A.L.; Hernández-Garrido, J.C.; Guerra, F.M.; Cifredo, G.A.; González-Leal, J.M.; Gatica, J.M. Low Temperature Prepared Copper-Iron Mixed Oxides for the Selective CO Oxidation in the Presence of Hydrogen. *Appl. Catal. A Gen.* **2018**, *552*, 58–69. [CrossRef]
43. Luo, M.-F.; Zhong, Y.-J.; Yuan, X.-X.; Zheng, X.-M. TPR and TPD Studies of $CuOCeO_2$ Catalysts for Low Temperature CO Oxidation. *Appl. Catal. A Gen.* **1997**, *162*, 121–131. [CrossRef]
44. Zhang, X.; Yang, Y.; Song, L.; Wang, Y.; He, C.; Wang, Z.; Cui, L. High and Stable Catalytic Activity of Ag/Fe 2 O 3 Catalysts Derived from MOFs for CO Oxidation. *Mol. Catal.* **2018**, *447*, 80–89. [CrossRef]
45. Perezalonso, F.; Meliancabrera, I.; Lopezgranados, M.; Kapteijn, F.; Fierro, J. Synergy of $Fe_xCe_{1-x}O_2$ Mixed Oxides for $N_2O$ Decomposition. *J. Catal.* **2006**, *239*, 340–346. [CrossRef]
46. Biesinger, M.C.; Lau, L.W.M.; Gerson, A.R.; Smart, R.S.C. Resolving Surface Chemical States in XPS Analysis of First Row Transition Metals, Oxides and Hydroxides: Sc, Ti, V, Cu and Zn. *Appl. Surf. Sci.* **2010**, *257*, 887–898. [CrossRef]
47. Espinós, J.P.; Morales, J.; Barranco, A.; Caballero, A.; Holgado, J.P.; González-Elipe, A.R. Interface Effects for Cu, CuO, and $Cu_2O$ Deposited on $SiO_2$ and $ZrO_2$. XPS Determination of the Valence State of Copper in $Cu/SiO_2$ and $Cu/ZrO_2$ Catalysts. *J. Phys. Chem. B* **2002**, *106*, 6921–6929. [CrossRef]
48. Kundakovic, L.; Flytzani-Stephanopoulos, M. Reduction Characteristics of Copper Oxide in Cerium and Zirconium Oxide Systems. *Appl. Catal. A Gen.* **1998**, *171*, 13–29. [CrossRef]
49. Yamashita, T.; Hayes, P. Analysis of XPS Spectra of $Fe^{2+}$ and $Fe^{3+}$ Ions in Oxide Materials. *Appl. Surf. Sci.* **2008**, *254*, 2441–2449. [CrossRef]
50. Weiss, W.; Ranke, W. Surface Chemistry and Catalysis on Well-Defined Epitaxial Iron-Oxide Layers. *Prog. Surf. Sci.* **2002**, *70*, 1–151. [CrossRef]
51. Wen, N.; Su, Y.; Deng, W.; Zhou, H.; Zhao, B. Selective Catalytic Reduction of NO with $C_3H_6$ over CuFe-Containing Catalysts Derived from Layered Double Hydroxides. *Fuel* **2021**, *283*, 119296. [CrossRef]
52. Dong, X.; Ren, B.; Sun, Z.; Li, C.; Zhang, X.; Kong, M.; Zheng, S.; Dionysiou, D.D. Monodispersed $CuFe_2O_4$ Nanoparticles Anchored on Natural Kaolinite as Highly Efficient Peroxymonosulfate Catalyst for Bisphenol A Degradation. *Appl. Catal. B Environ.* **2019**, *253*, 206–217. [CrossRef]
53. Carabineiro, S.A.C.; Chen, X.; Martynyuk, O.; Bogdanchikova, N.; Avalos-Borja, M.; Pestryakov, A.; Tavares, P.B.; Órfão, J.J.M.; Pereira, M.F.R.; Figueiredo, J.L. Gold Supported on Metal Oxides for Volatile Organic Compounds Total Oxidation. *Catal. Today* **2015**, *244*, 103–114. [CrossRef]
54. Saqer, S.M.; Kondarides, D.I.; Verykios, X.E. Catalytic Oxidation of Toluene over Binary Mixtures of Copper, Manganese and Cerium Oxides Supported on $\gamma$-$Al_2O_3$. *Appl. Catal. B Environ.* **2011**, *103*, 275–286. [CrossRef]
55. Durán, F.G.; Barbero, B.P.; Cadús, L.E.; Rojas, C.; Centeno, M.A.; Odriozola, J.A. Manganese and Iron Oxides as Combustion Catalysts of Volatile Organic Compounds. *Appl. Catal. B Environ.* **2009**, *92*, 194–201. [CrossRef]
56. Lutterotti, L.; Bortolotti, M.; Ischia, G.; Lonardelli, I.; Wenk, H.-R. Rietveld Texture Analysis from Diffraction Images. *Z. Kristallogr. Suppl.* **2007**, *26*, 125–130. [CrossRef]